Cingulo-opercular control network and disused motor circuits joined in standby mode

Dillan J. Newbold[a,1], Evan M. Gordon[b], Timothy O. Laumann[c], Nicole A. Seider[a], David F. Montez[a,c], Sarah J. Gross[a], Annie Zheng[a], Ashley N. Nielsen[a,d], Catherine R. Hoyt[e], Jacqueline M. Hampton[c], Mario Ortega[a], Babatunde Adeyemo[a], Derek B. Miller[a], Andrew N. Van[a,f], Scott Marek[a], Bradley L. Schlaggar[g,h,i], Alexandre R. Carter[a,e], Benjamin P. Kay[a], Deanna J. Greene[b,c], Marcus E. Raichle[a,b], Steven E. Petersen[a,b,f,j,k], Abraham Z. Snyder[a,b], and Nico U. F. Dosenbach[a,b,e,f,l,1]

[a]Department of Neurology, Washington University School of Medicine, St. Louis, MO 63110; [b]Department of Radiology, Washington University School of Medicine, St. Louis, MO 63110; [c]Department of Psychiatry, Washington University School of Medicine, St. Louis, MO 63110; [d]Institute for Innovations in Developmental Sciences, Northwestern University, Chicago, IL 60611; [e]Program in Occupational Therapy, Washington University School of Medicine, St. Louis, MO 63110; [f]Department of Biomedical Engineering, Washington University in St. Louis, St. Louis, MO 63110; [g]Kennedy Krieger Institute, Baltimore, MD 21205; [h]Department of Neurology, Johns Hopkins University School of Medicine, Baltimore, MD 21287; [i]Department of Pediatrics, Johns Hopkins University School of Medicine, Baltimore, MD 21287; [j]Department of Neuroscience, Washington University School of Medicine, St. Louis, MO 63110; [k]Department of Psychological and Brain Sciences, Washington University in St. Louis, St. Louis, MO 63110; and [l]Department of Pediatrics, Washington University School of Medicine, St. Louis, MO 63110

Edited by Peter L. Strick, University of Pittsburgh, Pittsburgh, PA, and approved February 11, 2021 (received for review September 10, 2020)

Whole-brain resting-state functional MRI (rs-fMRI) during 2 wk of upper-limb casting revealed that disused motor regions became more strongly connected to the cingulo-opercular network (CON), an executive control network that includes regions of the dorsal anterior cingulate cortex (dACC) and insula. Disuse-driven increases in functional connectivity (FC) were specific to the CON and somatomotor networks and did not involve any other networks, such as the salience, frontoparietal, or default mode networks. Censoring and modeling analyses showed that FC increases during casting were mediated by large, spontaneous activity pulses that appeared in the disused motor regions and CON control regions. During limb constraint, disused motor circuits appear to enter a standby mode characterized by spontaneous activity pulses and strengthened connectivity to CON executive control regions.

disuse | plasticity | fMRI | spontaneous activity | network neuroscience

Disuse is a powerful paradigm for inducing plasticity that has uncovered key organizing principles of the human brain (1–4). Monocular deprivation—prolonged covering of one eye—revealed that multiple afferent inputs can compete for representational territory in the primary visual cortex (1). Similar competition between afferents also shapes the somatomotor system. Manipulations such as peripheral nerve deafferentation, whisker trimming, and limb constraint all drive plasticity in the primary somatosensory and motor cortex (2–4). Most plasticity studies to date have used focal techniques, such as microelectrode recordings, to study local changes in brain function. As a result, little is known about how behavior and experience shape the brain-wide functional networks that support complex cognitive operations (5).

The brain is composed of networks of regions that cooperate to perform specific cognitive functions (5–8). These functional networks show synchronized spontaneous activity while the brain is at rest, a phenomenon known as resting-state functional connectivity (FC) (9–11). FC can be measured noninvasively in humans using resting-state functional MRI (rs-fMRI) and has been used to parse the brain into canonical functional networks (12, 13), including visual, auditory, and somatomotor networks (14, 15); ventral and dorsal attention networks (8, 16); a default mode network with roles in internally directed cognition and episodic memory (7, 11); a salience network thought to assess the homeostatic relevance of external stimuli (17); a frontoparietal control network supporting error processing and moment-to-moment adjustments in behavior (18–20); and a cingulo-opercular control network (CON), which maintains executive control during goal-directed behavior (18, 19, 21). Each functional network likely carries out a variety of additional functions.

A more recent advance in human neuroscience has been the recognition of individual variability in network organization (22–25). Most early rs-fMRI studies examined central tendencies in network organization using group-averaged FC measurements (10, 12, 13). Recent work has demonstrated that functional networks can be identified in an individual-specific manner if sufficient rs-fMRI data are acquired, an approach termed precision functional mapping (PFM) (22, 23, 26–30). PFM respects the unique functional anatomy of each person and avoids averaging together functionally distinct brain regions across individuals.

We recently demonstrated that PFM can be used to follow the time course of disuse-driven plasticity in the human brain (31). Three adult participants (Nico, Ashley, and Omar) were scanned at the same time of day for 42 to 64 consecutive days (30 min of rs-fMRI per day) before, during, and after 2 wk of dominant upper-extremity casting (Fig. 1 *A* and *B*). Casting caused persistent disuse of the dominant upper extremity during daily behaviors and led to

NEUROSCIENCE

Significance

Many studies have examined plasticity in the primary somatosensory and motor cortex during disuse, but little is known about how disuse impacts the brain outside of primary cortical areas. We leveraged the whole-brain coverage of resting-state functional MRI (rs-fMRI) to discover that disuse drives plasticity of distant executive control regions in the cingulo-opercular network (CON). Two complementary analyses, pulse censoring and pulse addition, demonstrated that increased functional connectivity between the CON and disused motor regions was driven by large, spontaneous pulses of activity appearing during disuse. These results point to a role for the CON in motor plasticity and reveal spontaneous activity pulses as a potential mechanism for maintaining and reorganizing the brain's functional connections.

Author contributions: D.J.N. and N.U.F.D. designed research; D.J.N. and N.U.F.D. performed research; D.J.N., E.M.G., and N.U.F.D. contributed new reagents/analytic tools; D.J.N., E.M.G., A.Z.S., and N.U.F.D. analyzed data; and D.J.N., E.M.G., T.O.L., N.A.S., D.F.M., S.J.G., A.Z., A.N.N., C.R.H., J.M.H., M.O., B.A., D.B.M., A.N.V., S.M., B.L.S., A.R.C., B.P.K., D.J.G., M.E.R., S.E.P., A.Z.S., and N.U.F.D. wrote the paper.

Competing interest statement: N.U.F.D. is a cofounder of NOUS Imaging.

This article is a PNAS Direct Submission.

Published under the PNAS license.

[1]To whom correspondence may be addressed. Email: newbold@wustl.edu or ndosenbach@wustl.edu.

This article contains supporting information online at https://www.pnas.org/lookup/suppl/doi:10.1073/pnas.2019128118/-/DCSupplemental.

Published March 22, 2021.

Downloaded at Palestinian Territory, occupied on November 29, 2021

www.manaraa.com

a marked loss of strength and fine motor skill in all participants. During casting, the upper-extremity regions of the left primary somatomotor cortex (L-SM1$_{ue}$) and right cerebellum (R-Cblm$_{ue}$) functionally disconnected from the remainder of the somatomotor network. Disused motor circuits also exhibited large, spontaneous pulses of activity (Fig. 1*C*). Disuse pulses did not occur prior to casting, started to occur frequently within 1 to 2 d of casting, and quickly waned after cast removal.

Somatomotor circuits do not function in isolation. Action selection and motor control are thought to be governed by complex interactions between the somatomotor network and control networks, including the CON (18). Prior studies of disuse-driven plasticity, including our own, have focused solely on somatomotor circuits. Here, we leveraged the whole-brain coverage of rs-fMRI and the statistical power of PFM to examine disuse-driven plasticity throughout the human brain.

Results

Disuse Caused Both Increases and Decreases in Functional Connectivity. To examine disuse-driven plasticity beyond somatomotor networks, we first generated seed maps showing FC between L-SM1$_{ue}$ and all other cortical regions before, during, and after casting (Fig. 2*A* and *SI Appendix*, Fig. S1). Prior to casting (Pre), L-SM1$_{ue}$ was strongly connected to the remainder of the somatomotor cortex (pre- and postcentral gyri), especially homotopic R-SM1$_{ue}$. During the cast period (Cast), L-SM1$_{ue}$ showed a new pattern of connectivity, with strong connections to the bilateral secondary somatosensory cortex (SII), dorsal anterior cingulate cortex (dACC), and pre- and postcentral sulci. After casting (Post), L-SM1$_{ue}$ FC returned to baseline. Changes in FC during casting (Cast − Pre) and recovery (Post − Cast) were examined using previously published sets of individual-specific cortical parcels (22, 31). Casting caused decreased L-SM1$_{ue}$ connectivity with the remainder of the somatomotor cortex, as well as increased connectivity with the bilateral SII, dACC, and pre- and postcentral sulci (Fig. 2*B* and *SI Appendix*, Fig. S1). FC changes after cast removal were strongly negatively correlated with changes during casting (Nico: spatial correlation, $r = -0.56$; Ashley: $r = -0.95$; Omar: $r = -0.32$; all participants: $P < 0.001$), indicating that most effects reversed after cast removal (Fig. 2*B* and *SI Appendix*, Fig. S1).

Disuse-Driven Functional Connectivity Changes Were Highly Focal in Network Space. The brain's functional network organization can be visualized using spring-embedded graphs, which treat functional

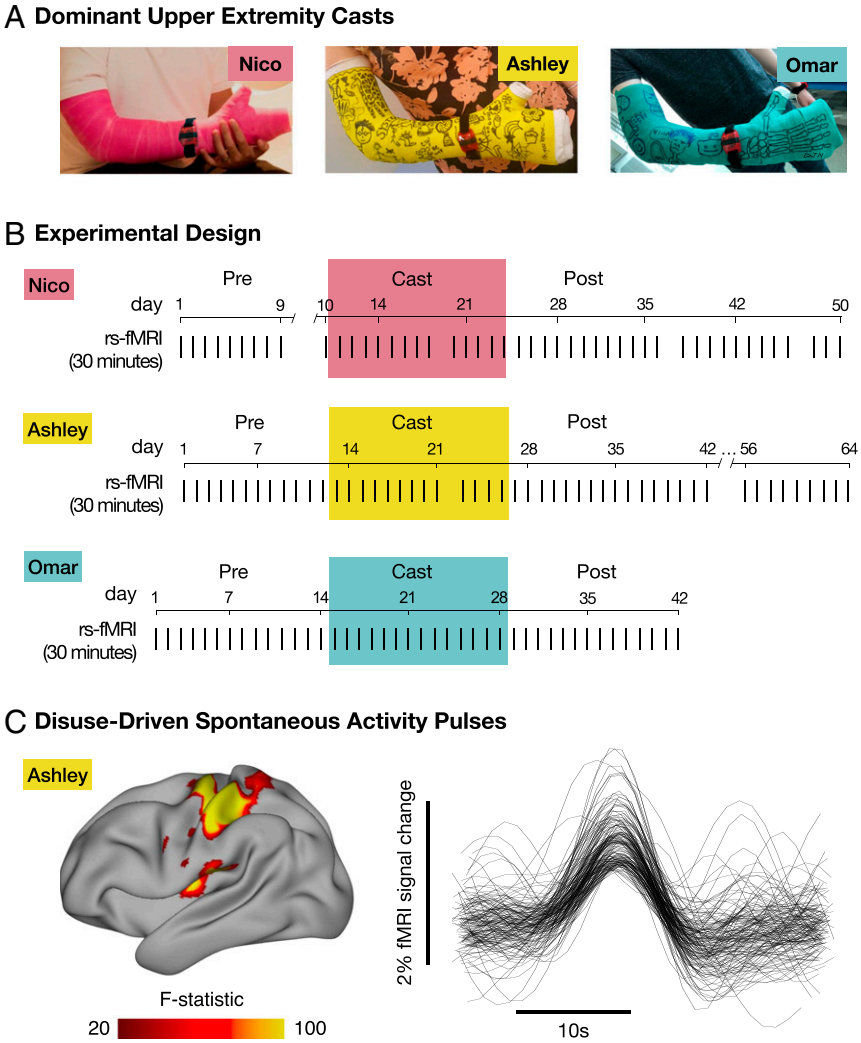

Fig. 1. Experimental design and spontaneous activity pulses. (*A*) Three participants (Nico, Ashley, and Omar) wore casts covering the entire dominant upper extremity for 2 wk. (*B*) Participants were scanned every day for 42 to 64 consecutive days before, during, and after casting. All scans included 30 min of resting-state functional MRI. (*C*) During the Cast period, disused somatomotor circuits exhibited large pulses of spontaneous activity. (*C*, *Left*) Whole-brain ANOVA showing which brain regions contained disuse-driven pulses. (*C*, *Right*) Time courses of all pulses recorded from the disused primary somatomotor cortex.

Downloaded at Palestinian Territory, occupied on November 29, 2021

www.manaraa.com

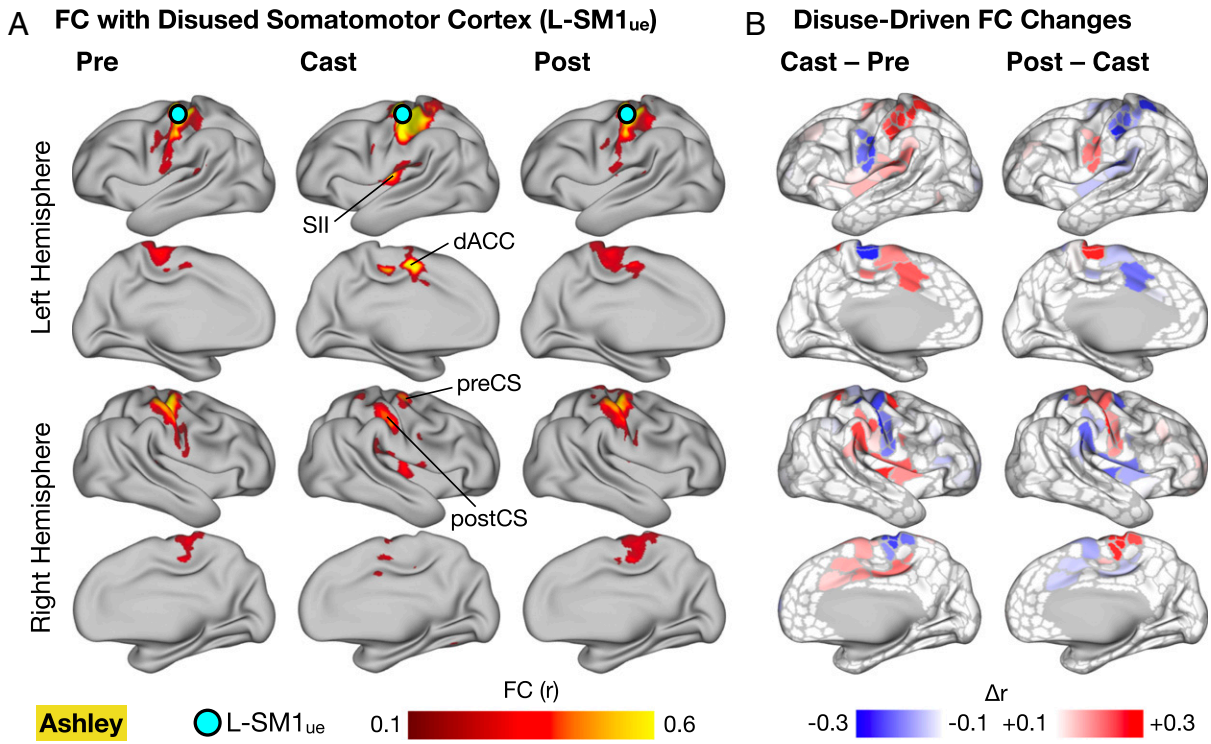

Fig. 2. Cast-driven changes in functional connectivity of disused somatomotor cortex (L-SM1$_{ue}$). (*A*) Seed maps showing FC between L-SM1$_{ue}$ and the remainder of the cerebral cortex in an example participant (Ashley; remaining participants are shown in *SI Appendix*, Fig. S1). Seed maps were averaged across sessions before, during, and after casting. Labels indicate secondary somatosensory cortex, dorsal anterior cingulate cortex, and pre- and postcentral sulci (preCS and postCS). (*B*) Subtraction maps showing changes in FC during casting (Cast − Pre) and recovery (Post − Cast). Differences are shown on a set of previously published individual-specific cortical parcels (21).

connections as spring forces, positioning more strongly connected nodes closer to one another (Fig. 3*A* and *SI Appendix*, Fig. S2). While L-SM1$_{ue}$ FC increases were widely distributed in anatomical space, including regions on the medial and lateral surfaces of both hemispheres, nearly all of these changes mapped onto a single cluster in network space, the CON (Fig. 3*B* and *SI Appendix*, Fig. S2). The network focality of L-SM1$_{ue}$ FC increases was quantified by examining the distribution of the greatest FC increases (top 5%) across the canonical functional networks (Fig. 3*B*). In all participants, the CON showed more FC increases than expected by chance ($P < 0.001$ for all participants), independent of the chosen FC threshold (*SI Appendix*, Fig. S3). Decreases in L-SM1$_{ue}$ FC were also localized in network space (Fig. 3*C* and *SI Appendix*, Figs. S2 and S3). Most of the regions showing decreased FC with L-SM1$_{ue}$ during casting belonged to the somatomotor networks (upper-extremity somatomotor network [ue-SMN], lower-extremity SMN [le-SMN], face SMN [f-SMN], and premotor network). All participants showed more FC decreases than expected by chance in the ue-SMN ($P < 0.001$ for all participants). Additionally, two participants (Ashley and Omar) showed significant FC decreases in other somatomotor networks, including the le-SMN, f-SMN, and premotor network.

Plasticity Was Restricted to the Somatomotor and Cingulo-Opercular Networks. The analyses presented thus far focus on changes in connectivity between L-SM1$_{ue}$ and the remainder of the cerebral cortex. To examine whole-brain patterns of FC changes induced by casting, we extracted rs-fMRI signals from individual-specific cortical, subcortical, and cerebellar parcels (Nico: 744 parcels; Ashley: 733; Omar: 761) and examined FC changes in all possible pairwise connections (*SI Appendix*, Fig. S4). We displayed the 50 largest changes in FC (25 greatest increases and 25 greatest decreases) in anatomical space (Fig. 4*A* and *SI Appendix*, Fig. S3). Disuse-driven FC changes were largely restricted to connections involving L-SM1$_{ue}$ and the CON. Fig. 4*B* shows the total magnitude of whole-brain FC change for each vertex/voxel in the brain. The total magnitude of whole-brain FC change was significantly greater in L-SM1$_{ue}$ than in the remainder of the brain (Fig. 4*B* and *SI Appendix*, Fig. S4; Nico: $P = 0.021$; Ashley: $P < 0.001$; Omar: $P = 0.005$).

Increased Connectivity with the CON Depended on a Recent History of Disuse. To distinguish between increases in connectivity due to wearing a cast during MRI scans (i.e., an altered behavioral state) and increases in connectivity due to a history of having been casted (i.e., disuse-driven plasticity), we conducted a control experiment in which participants wore casts during 30-min scans but were not casted during their daily lives. In both cases, we compared FC between L-SM1$_{ue}$ and the left dorsal anterior cingulate cortex (L-dACC; *SI Appendix*, Fig. S5*A*), in cast and no-cast conditions. The L-dACC is a core node within the CON (21). As suggested by the whole-brain network analyses (Fig. 3*B*), FC between L-SM1$_{ue}$ and L-dACC was significantly increased during the cast period (*SI Appendix*, Fig. S5*B*). When participants wore casts during scans but were not casted during their daily lives, no changes in FC were observed (*SI Appendix*, Fig. S5*C*). This control experiment indicated that increased FC between the disused motor circuitry and the CON depended on participants' recent history of disuse, not their current state of casting.

Network-Specific Connectivity Changes Reflect Spontaneous Activity Pulses. Increases in FC with L-SM1$_{ue}$ showed a similar anatomical distribution to the spontaneous activity pulses we described previously (31) (*SI Appendix*, Fig. S6 *A* and *B*). Additionally, FC

NEUROSCIENCE

Downloaded at Palestinian Territory, occupied on November 29, 2021

www.manaraa.com

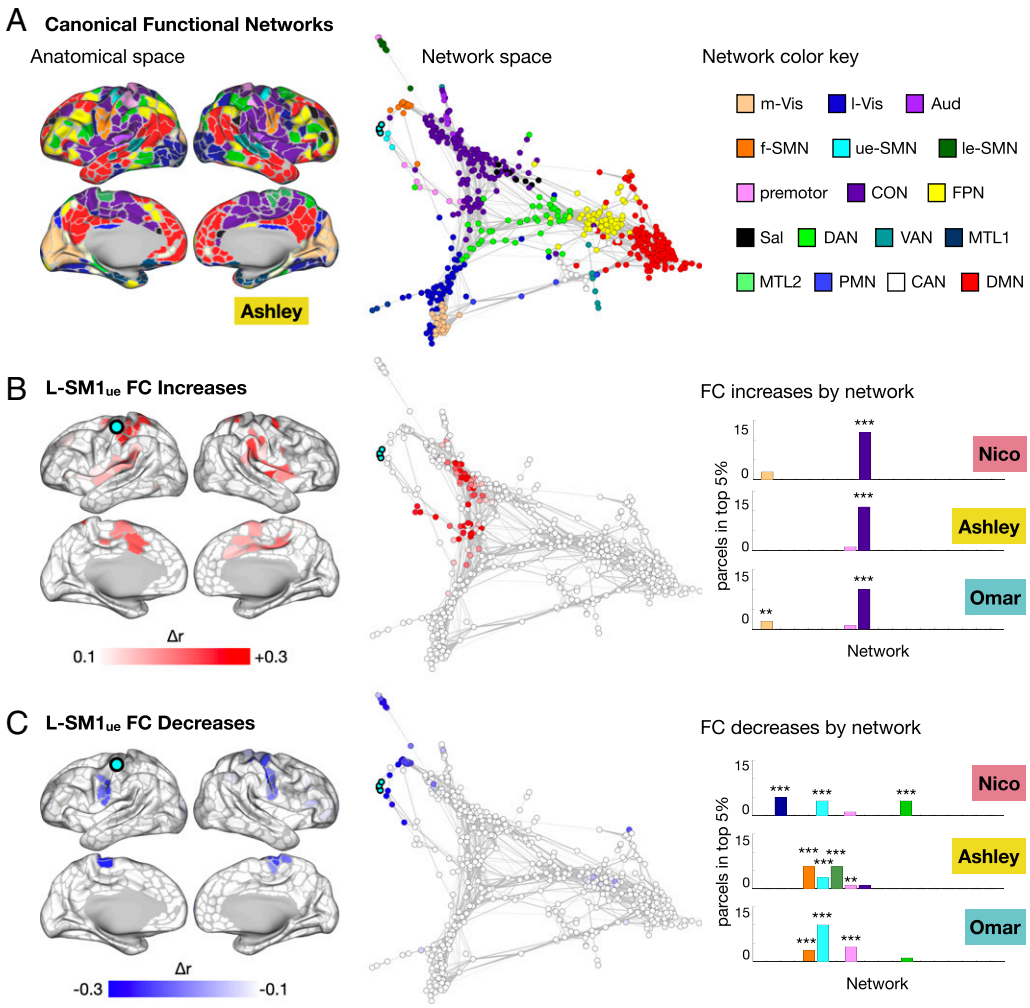

Fig. 3. Disused somatomotor cortex (L-SM1$_{ue}$) FC changes in network space. (*A*) Map of canonical functional networks in an example participant (Ashley; remaining participants are shown in *SI Appendix*, Fig. S1). (*A*, *Left*) Networks shown in anatomical space (inflated cortical surfaces). (*A*, *Middle*) Same map as *Left*, shown in network space (spring-embedded graphs based on Pre scans). (*A*, *Right*) Network color key: Aud, auditory; CAN, context association; DAN, dorsal attention; DMN, default mode; FPN, frontoparietal; l-Vis, lateral visual; MTL: medial temporal lobe; m-Vis, medial visual; PMN, parietal memory; Sal, salience; VAN, ventral attention. (*B*, *Left*) Subtraction maps showing disuse-driven decreases in FC with L-SM1$_{ue}$ in anatomical space. (*B*, *Middle*) Same map as *Top*, shown in network space. (*B*, *Right*) Distribution of the top 5% FC decreases across all networks. $^{**}P < 0.01$, $^{***}P < 0.001$; FDR < 0.05. (*C*) Subtraction maps showing disuse-driven increases in FC with L-SM1$_{ue}$ in anatomical (*Left*) and network space (*Middle*). (*C*, *Right*) Distribution of the top 5% FC increases across all networks.

between L-SM1$_{ue}$ and the CON was highly correlated with the number of pulses detected in L-SM1$_{ue}$ during each scan (*SI Appendix*, Fig. S6*C*; Nico: $r = 0.74$; Ashley: $r = 0.57$; Omar: $r = 0.73$; all participants: $P < 0.001$). These observations led us to suspect that FC between L-SM1$_{ue}$ and the CON was increased during the cast period because both regions showed synchronized spontaneous activity pulses.

To test if spontaneous activity pulses could explain observed increases in FC, we implemented a pulse censoring strategy, in which frames surrounding each detected pulse (13.2 s before to 17.6 s after each pulse peak) were excluded from FC calculations (Fig. 5*A*). This approach is similar to the censoring strategy commonly used to correct the effects of head motion on FC (32). Censoring pulses partially reduced the FC changes observed during casting (Fig. 5*B*; Nico: −55%, $P = 0.28$; Ashley: −28%, $P = 0.04$; Omar: −21%, $P = 0.08$). Additionally, the spatial pattern of FC changes caused by pulse censoring (censored − uncensored; Fig. 5*C* and *SI Appendix*, Fig. S7) was negatively correlated with FC changes during casting (Nico: $r = -0.35$; Ashley: $r = -0.90$; Omar: $r = -33$; all participants: $P < 0.001$).

Censoring pulses did not entirely eliminate the effect of casting on FC. The residual effect of casting after pulse censoring was negatively spatially correlated with the effects of pulse censoring (*SI Appendix*, Fig. S7; Nico: spatial correlation, $r = -0.23$; Ashley: $r = -0.76$; Omar: $r = -0.18$; all participants: $P < 0.001$), suggesting that the residual effect may have been driven by additional pulses that were too small to distinguish from ongoing spontaneous activity fluctuation. Pulses showed a wide distribution of magnitudes (Fig. 6*A*; range: 0.4 to 1.2% rs-fMRI signal change). Because pulses were detected using a threshold-based approach (31), pulses smaller than 0.4% fMRI signal change could not be detected and censored. To test if smaller pulses that escaped detection could explain the residual increased FC between L-SM1$_{ue}$ and L-dACC after pulse censoring, we simulated a full distribution of pulse magnitudes by adding the mean pulse time series from L-SM1$_{ue}$ and L-dACC to the baseline rs-fMRI signals recorded from these regions prior to casting (Fig. 6*B*). Simulated pulse magnitudes were drawn from a log-normal distribution, fit to the magnitude distribution of detected pulses using a least-squares approach (Fig. 6*A*; see *SI Appendix*, Fig. S8 for triangular and

Downloaded at Palestinian Territory, occupied on November 29, 2021

www.manaraa.com

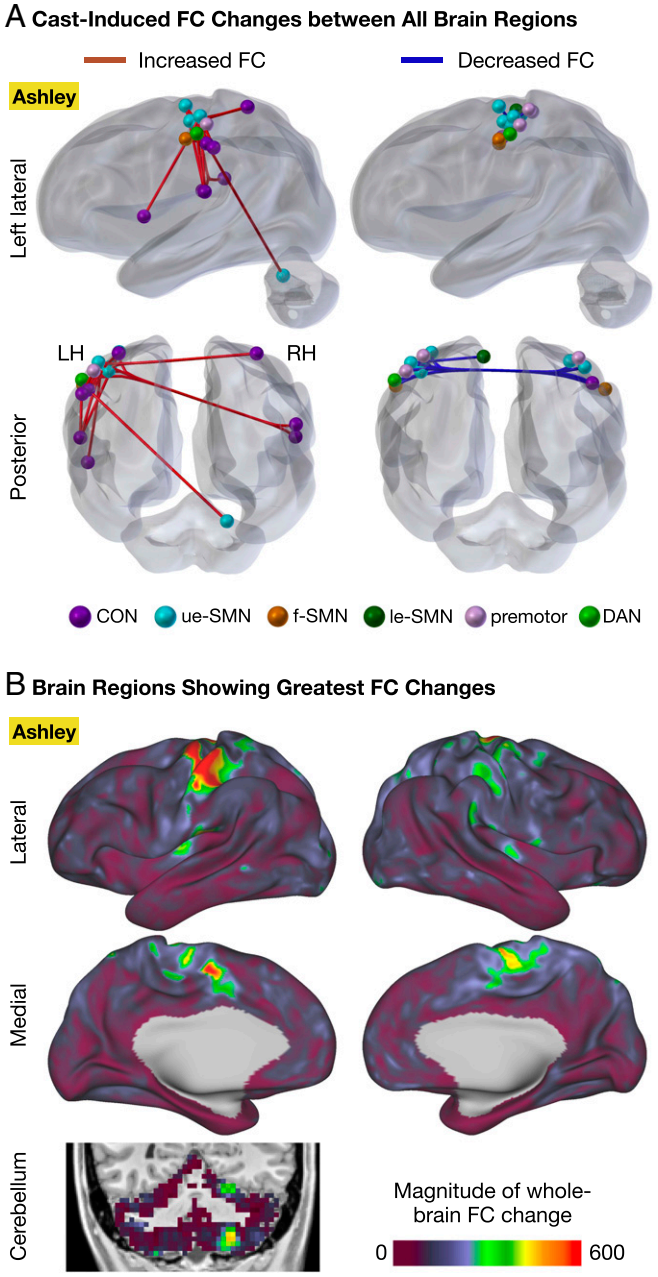

Fig. 4. Whole-brain analyses of disuse-driven FC changes. (*A*) Changes in FC were computed for all pairs of cortical, subcortical, and cerebellar parcels (mean Cast FC − mean Pre FC). The 50 most altered functional connections (top 25 increases and top 25 decreases) are shown for an example participant (Ashley; all participants are shown in *SI Appendix*, Fig. S4). LH, left hemisphere; RH right hemisphere. (*B*) For each vertex/voxel, the magnitude of whole-brain FC change was computed as the sum of squared FC changes between that vertex and every other gray-matter vertex/voxel. Shown for an example participant (Ashley; all participants are shown in *SI Appendix*, Fig. S4).

exponential distributions). Adding simulated pulses caused FC increases with a similar effect size (Nico: $\Delta r = +0.07$, $P = 0.013$; Ashley: $\Delta r = +0.40$, $P < 0.001$; Omar: $\Delta r = +0.19$, $P < 0.001$) to the FC increases observed during casting (Fig. 6*C*). The FC effects of adding simulated pulses did not differ significantly from those of casting (Nico: $\Delta r = -0.02$, $P = 0.53$; Ashley: $\Delta r = +0.09$, $P = 0.08$; Omar: $\Delta r = -0.05$, $P = 0.13$). Applying the same pulse censoring strategy described above to the simulated pulses partially reduced the increases in FC (Fig. 6*C*; Nico: −79%; Ashley: −58%; Omar: −69%; all participants: $P < 0.001$), similar to the effect of pulse censoring on the actual data (Fig. 5*B*). Adding simulated pulses to all brain regions, using mean pulse time series specific to each region (*Methods*), recreated the anatomical distribution of FC changes observed during casting (Fig. 6*D* and *SI Appendix*, Fig. S9; Nico: $r = 0.44$; Ashley: $r = 0.95$; Omar: $r = 0.64$; all participants: $P < 0.001$). Thus, pulses with a full distribution of magnitudes could account for observed FC changes during casting and the partial reversal of FC changes after pulse censoring.

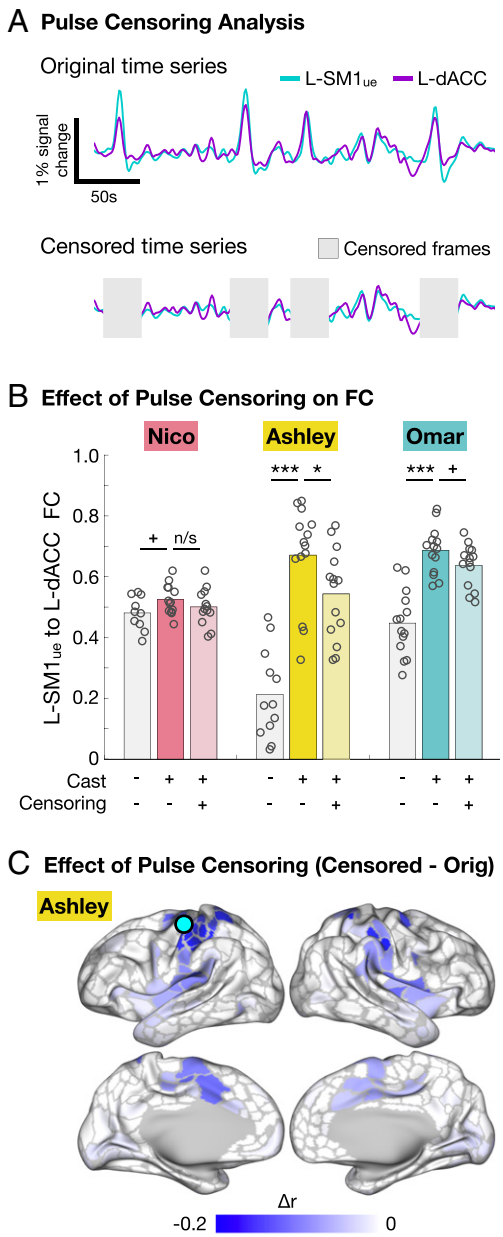

Fig. 5. Censoring pulses from FC measurements. (*A*) Schematic explaining the censoring approach used to remove detected pulses from FC calculation. (*B*) Censoring pulses partially reduced the difference between Pre and Cast scans. $^{+}P < 0.1$, $^{*}P < 0.05$, $^{***}P < 0.001$; n/s, not significant. (*C*) Subtraction map showing reductions in L-SM1$_{ue}$ FC due to pulse censoring. The spatial pattern of FC changes due to pulse censoring was significantly negatively correlated with FC changes during casting (Nico: $r = -0.35$; Ashley: $r = -0.90$; Omar: $r = -0.33$; all participants: $P < 0.001$).

Downloaded at Palestinian Territory, occupied on November 29, 2021

www.manaraa.com

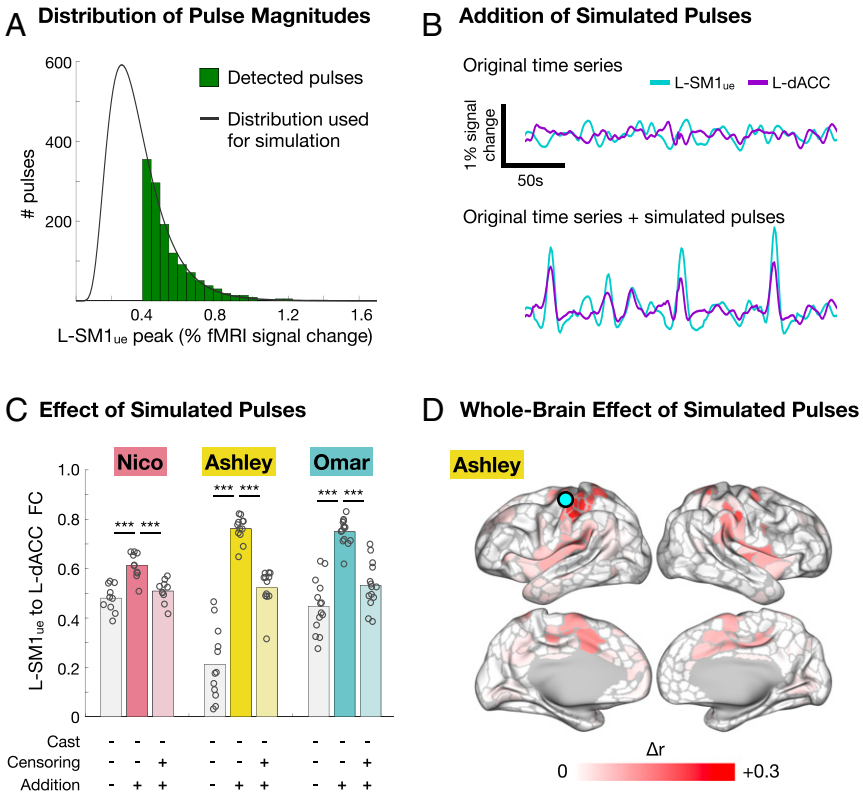

Fig. 6. Addition of simulated pulses. (*A*) Histogram of pulse magnitudes (peak fMRI signal), pooled across participants. A log-normal distribution (black line) was fit to the data using a least-squares approach. (*B*, *Top*) Example rs-fMRI signals from disused motor cortex (L-SM1$_{ue}$) and L-dACC recorded prior to casting (Pre). (*B*, *Bottom*) Same time series with simulated pulses added at random time points. Simulated pulse magnitudes were drawn from the full distribution shown in *A*. (*C*) Adding simulated pulses increased FC between L-SM1$_{ue}$ and L-dACC (***$P < 0.001$). Censoring simulated pulses partially reduced FC increases (***$P < 0.001$). (*D*) Subtraction map showing increases in L-SM1$_{ue}$ FC caused by simulated pulses in an example participant (Ashley; all participants are shown in *SI Appendix*, Fig. S8). N.B. Simulated pulses added to each region were based on region-specific mean pulse time courses (*Methods*).

To ensure that the L-dACC connectivity changes detailed above were representative of the CON as a whole, we repeated the pulse censoring and pulse addition analyses examining FC changes between L-SM1$_{ue}$ and the left anterior insula (L-insula), another core region of the CON. The L-insula FC analyses yielded similar results to those for the L-dACC (*SI Appendix*, Fig. S10). We also utilized the pulse censoring and pulse addition analyses to test if pulses could explain previously reported decreases in FC within the somatomotor system (31). Pulse censoring did not significantly reverse the decrease in FC between L-SM1$_{ue}$ and R-SM1$_{ue}$ observed during the cast period (*SI Appendix*, Fig. S10). Adding simulated pulses to baseline time series decreased FC between L-SM1$_{ue}$ and R-SM1$_{ue}$, but this effect was much smaller than that observed during casting (*SI Appendix*, Fig. S10).

Discussion

Disuse Drives Plasticity of Functional Networks. Daily 30-min scans of rs-fMRI before, during, and after casting revealed that disuse not only causes plasticity within the primary motor cortex (3, 31) but also increases functional connectivity between disused circuits and executive control regions in the CON. These increases in FC would have been difficult to observe using the focal recording techniques traditionally employed to study plasticity. Thus, understanding the total impact of disuse on brain function requires consideration of plasticity at multiple spatial scales.

The high degree of network specificity seen in disuse-driven plasticity is a powerful demonstration of the validity of rs-fMRI network parcellations. It could have been the case that casting produced a complex pattern of FC changes involving many brain systems. Instead, we found that virtually all of the regions showing increased connectivity with the disused motor cortex belonged to a single network, the CON. Thus, large-scale functional networks seem to be a fundamental unit of brain organization, important not only for understanding patterns of activation during cognitive processes but also for understanding whole-brain patterns of plasticity.

Spontaneous Activity Pulses Alter Functional Connectivity. The network-specific increases in FC between the disused L-SM1$_{ue}$ and the CON likely reflect the emergence of synchronized spontaneous activity pulses in these regions during casting. FC is a measurement of the temporal correlation of spontaneous activity between brain regions. Two complementary analyses (pulse censoring and pulse addition) suggested that pulses contributed to increases in measured FC between disused motor regions and the CON. Many studies have reported increased FC in neuropsychiatric conditions, for example, Parkinson's disease (33) and major depressive disorder (34). Perhaps some previously reported FC increases could reflect spontaneous activity pulses, similar to those caused by limb disuse, especially since our analyses suggest that even pulses too small to be separated from the background signal fluctuations could alter FC. Going forward, spontaneous activity pulses, and the network-specific FC changes they produce, could serve as a biomarker of recent disuse and states of heightened plasticity.

Decreases in connectivity within the somatomotor system were not fully explained by spontaneous activity pulses. Although the pulse addition analyses showed that spontaneous activity pulses

Downloaded at Palestinian Territory, occupied on November 29, 2021

www.manaraa.com

could contribute to decreases in connectivity observed during casting, both the pulse censoring and pulse addition analyses suggested that at least part of the observed decrease in connectivity occurred independent of pulses. Loss of typical coactivation of L-SM1$_{ue}$ and R-SM1$_{ue}$ during daily behavior (31) likely contributed to cast-driven connectivity decreases, consistent with the widely held hypothesis that FC is maintained by a Hebbian-like mechanism that depends on coactivation of brain regions during behavior (19, 35–38).

Disuse Impacts the Cingulo-Opercular Network Important for Executive Control. The importance of control systems in the human brain has been recognized for several decades (6), but our understanding of these systems has changed dramatically over time and continues to evolve (39). Disentangling the roles of two networks mediating executive control, the cingulo-opercular and frontoparietal networks, has relied largely on complex task designs such as task-switching (21) and slow-reveal paradigms (40). Here, we have demonstrated that whole-brain precision functional mapping combined with anatomically specific disuse paradigms can shed light on the network interactions that support human cognition and behavior. Although the brain contains several suspected control networks beyond the CON, such as the frontoparietal, dorsal attention, ventral attention, and salience networks, disused motor regions showed increased FC only with the CON. The CON is thought to initiate goal-directed behaviors and maintain executive control settings in relation to task objectives (18, 19). The increased FC between disused L-SM1$_{ue}$ and the CON during casting suggests either 1) circuits within the CON were also disused during casting, 2) the CON helps to maintain disused motor circuitry, or 3) spontaneous activity pulses can spread along functional connections to neighboring brain regions in network space.

Spontaneous activity pulses may have emerged in the CON because its use was also reduced during casting. We previously suggested that spontaneous activity pulses found in motor regions may have been caused by disuse-driven changes in local inhibitory physiology (31, 41). The CON is generally thought to represent task sets, abstract parameters, and motor programs governing goal-driven behaviors (18, 19). Task sets can be applied to multiple motor effectors (e.g., right hand, left index finger, etc.), so it would be reasonable to think that casting one extremity would not cause disuse of the CON. However, at least two sets of circuits within the CON may have been disused during casting: circuits that represent bimanual behaviors and circuits that convey task sets to effector-specific downstream regions (e.g., L-SM1$_{ue}$). During casting, many of the task sets previously used to control the dominant upper extremity (e.g., inserting a key into a lock) could have been used to control the nondominant extremity. However, task sets requiring bimanual coordination (e.g., fastening a belt) could not be applied to an alternative set of motor effectors and may have become disused. Another set of CON circuits that may have been disused are the circuits that convey task set information to effector-specific brain regions. The CON contains both somatotopically organized regions (e.g., dACC, SII) and nonsomatotopic regions (e.g., anterior insula). Recent work shows that the dACC and SII, as well as regions of the basal ganglia, may act as hubs that connect the rest of the CON to the somatomotor network (27, 42). Such circuits could potentially undergo disuse during casting of one extremity.

An alternative possibility is that inputs from the CON to L-SM1$_{ue}$ served a homeostatic function during disuse, helping to maintain motor circuits that are typically maintained through active use. We previously suggested that spontaneous activity pulses may help to maintain the organization of disused brain circuits (31). Perhaps pulses are triggered by the CON, which is the system typically responsible for initiating activation of the somatomotor network (18).

Spontaneous activity pulses may also have originated in the disused somatomotor circuits and spread along functional connections to brain regions that were not affected by casting. The CON is immediately adjacent to the somatomotor network in network space (Fig. 3*A*). Previous work in mice found that spontaneous activity bursts in the somatosensory cortex, caused by pharmacogenetic suppression of local inhibitory interneurons, spread to other functionally connected regions not targeted by the experimental manipulation (43). An interesting question for future research is whether the CON would show spontaneous activity pulses following disuse of brain systems other than the somatomotor network, such as networks supporting visual and auditory processing, spatial navigation, or social cognition.

Two Complementary Mechanisms for Functional Network Plasticity. Extensive whole-brain imaging before, during, and after casting revealed that disuse-driven spontaneous activity pulses occur not only in primary motor and somatosensory areas but also in higher-order brain regions responsible for executive control over behavior. The emergence of spontaneous activity pulses during casting produced increases in FC that were highly focal in network space, specifically occurring between disused motor regions and the CON. Decreases in connectivity between disused motor circuits and the remainder of the somatomotor system, however, were not explained by spontaneous activity pulses. Thus, disuse may drive network plasticity through two complementary mechanisms. Decreased coactivation of brain regions during disuse might drive Hebbian-like disconnection between disused and still-active somatomotor circuits. Spontaneous activity pulses, which contributed to increased connectivity with the CON, may help preserve disused circuits for future reintegration and use. Together, these two network plasticity mechanisms—Hebbian-like and pulse-mediated—may represent a network-focal "standby mode" that allows the brain to isolate disused circuits while simultaneously protecting them from premature functional degradation.

Methods

Human Participants. Participants were three healthy adult volunteers. The first participant (Nico) was 35 y old at the time of scanning and is male. The second participant (Ashley) was 25 y old and female. The third participant (Omar) was 27 y old and male. All participants were right-handed. The Washington University School of Medicine Institutional Review Board approved the study protocol and provided experimental oversight. Participants provided informed consent for all aspects of the study and were paid for their participation.

Experimental Intervention. We constrained the dominant upper extremity for 2 wk by fitting each participant with a fiberglass cast. Casts extended from just below the shoulder to past the fingertips. After the original experiment, we performed a control experiment in which participants were scanned 12 to 24 additional times and wore removable casts during half of the scanning sessions but were not casted during daily activities. Details of cast construction are described in Newbold et al. (31).

MRI Acquisition. Participants were scanned every day of the experiment for 42 to 64 consecutive days. We collected 30 min of resting-state functional MRI data every day of the experiment, as well as task fMRI and T1- and T2-weighted structural scans. Acquisition parameters and procedures are detailed in Newbold et al. (31).

MR Image Processing. Preprocessing of structural and functional images, denoising of resting-state fMRI data, and cortical surface projection were performed previously (31). Functional image processing followed a previously published pipeline (44) and involved temporal interpolation to correct for differences in slice acquisition timing, rigid-body correction of head movements, correction for susceptibility inhomogeneity-related distortions, and alignment to atlas space (711-2b implementation of Talairach space). Denoising involved replacement of high-motion frames (framewise displacement [FD] > 0.1 mm or variance of derivatives > 6% rms) by temporal linear interpolation, band-pass filtering (0.005 to 0.1 Hz), and regression of nuisance time series, including head movement parameters, the global signal averaged across all gray-matter voxels, and orthogonalized waveforms extracted from ventricles, white matter, and extracranial tissues. There were no systematic differences in head movement (mean FD or number of frames removed) between experimental conditions. Cortical surface projection

NEUROSCIENCE

Downloaded at Palestinian Territory, occupied on November 29, 2021

www.manaraa.com

utilized individual-specific surfaces defining the cortical gray-matter boundaries derived from T1-weighted images using FreeSurfer (45). Cortical surface data were smoothed using a two-dimensional 6-mm full-width half-maximum (FWHM) smoothing kernel and volume data were smoothed using a three-dimensional 4.7-mm FWHM kernel. Fully processed data are available in the Derivatives folder of the Cast-Induced Plasticity dataset in OpenNeuro (https://openneuro.org/datasets/ds002766).

ROI Selection. The region of interest (ROI) in L-SM1$_{ue}$ was located individually in each participant using an automated analysis of task fMRI, as previously described (26, 31). We selected ROIs inside the left primary somatomotor cortex (pre- and postcentral gyri), as automatically labeled by FreeSurfer (45). We first located the vertex within the left somatomotor cortex showing maximal task synchrony (26) during the right-hand movement and then grew the ROI to a preset size (400 vertices) by selecting neighboring vertices in descending order of task synchrony. The L-SM1$_{ue}$ ROI was used here to generate seed maps (Fig. 2 and *SI Appendix*, Fig. S1), analyze spatial specificity of whole-brain functional connectivity changes (Fig. 4*B* and *SI Appendix*, Fig. S4), and measure FC between L-SM1$_{ue}$ and dACC for the removable cast control experiment (*SI Appendix*, Fig. S5), pulse censoring analysis (Fig. 5), and pulse addition analysis (Fig. 6 and *SI Appendix*, Fig. S8).

Individual-specific sets of parcels spanning the entire cerebral cortex were previously generated for each participant using a functional connectivity gradient-based approach (22, 31). In all participants, parcellations utilized data acquired prior to casting. For Nico and Ashley, parcels were previously generated and published as part of the Midnight Scan Club experiment (22). For Omar, parcels were generated based on precast scans acquired during the current experiment (31). Individual-specific parcellations generated a different number of parcels in each participant and there was no one-to-one correspondence of parcels between participants. In order to compare results across participants, each parcel was assigned to one of 17 canonical functional networks using a graph theory-based community detection algorithm and anatomical priors (22, 31). Cortical parcels were used here to display functional connectivity changes in anatomical (Figs. 2, 3, and 6 and *SI Appendix*, Figs. S1, S2, and S5–S7) and network space (Fig. 3 and *SI Appendix*, Fig. S2). We also generated a set of subcortical and cerebellar parcels by assigning each voxel to the functional network with which it showed the strongest functional connectivity and then grouping adjacent voxels with matching network assignments into parcels. Sets of cortical, subcortical, and cerebellar parcels were used to examine changes in FC between all pairs of brain regions (Fig. 4 and *SI Appendix*, Fig. S4).

A subset of parcels corresponding to L-SM1$_{ue}$ was previously generated by selecting all left-hemisphere parcels assigned to the upper-extremity somatomotor network, excluding any parcels that fell outside of the pre- and postcentral gyri (31). Functional connections between L-SM1$_{ue}$ parcels and all other parcels were averaged to generate parcel-wise seed maps (Figs. 2, 3, and 6 and *SI Appendix*, Figs. S1, S2, and S5–S7).

Individual-specific ROIs in L-dACC and L-insula were selected using pulse ANOVA maps, which were previously generated for each participant (31). ROIs were selected within large anatomical regions in the medial prefrontal cortex (union of the caudal anterior cingulate gyrus, posterior cingulate gyrus, and superior frontal gyrus) and anterior insula (pars opercularis), automatically labeled by FreeSurfer. We first located the vertex within each anatomical region showing the maximum ANOVA *F* statistic and then iteratively expanded the ROIs by selecting neighboring vertices in descending order of *F* statistic, until each ROI included 100 vertices. The L-dACC ROI was used to measure FC between L-SM1$_{ue}$ and L-dACC for pulse censoring (Fig. 5) and pulse addition analyses (Fig. 6 and *SI Appendix*, Fig. S8). The L-insula ROI was used to measure FC between L-SM1$_{ue}$ and L-insula for pulse censoring and pulse addition analyses (*SI Appendix*, Fig. S10).

Functional Connectivity Measurement. Mean rs-fMRI time series were extracted from the L-SM1$_{ue}$ ROI and each cortical, subcortical, and cerebellar parcel by averaging the time series of all vertices/voxels within the ROI/parcel. Vertex-wise FC seed maps were generated for each session by computing a Pearson correlation between the mean rs-fMRI time series from the L-SM1$_{ue}$ ROI and the time series from every vertex. Frames with high head motion, identified previously (31), were excluded from FC calculations. Vertex-wise seed maps were averaged across sessions before, during, and after casting (Pre, Cast, and Post; Fig. 2 and *SI Appendix*, Fig. S1).

FC between all pairs of cortical, subcortical, and cerebellar parcels was measured as pairwise correlations of all mean rs-fMRI time series, excluding high-motion frames, producing a correlation matrix for each session. Correlation matrices were averaged over Pre, Cast, and Post periods. FC changes during casting and recovery were computed as the differences between correlation matrices (casting = Cast − Pre; recovery = Post − Cast). Full Cast − Pre difference matrices are shown in *SI Appendix*, Fig. S4. Parcel-wise difference seed maps showing changes in L-SM1$_{ue}$ FC during casting and recovery (Figs. 2 and 3 and *SI Appendix*, Figs. S1 and S2) were computed by averaging together columns of the difference matrices corresponding to the L-SM1$_{ue}$ parcels (*ROI Selection*).

Spring Embedding. Cortical parcels were displayed in network space using force-directed ("spring-embedded") graphs (46), generated with Gephi (https://gephi.org/). Graph weights were taken from parcel-wise correlation matrices averaged across all sessions prior to casting (Pre). Graphs were thresholded to include only the top 0.2% of pairwise functional connections. We initially examined graphs using an edge threshold of 0.1%, but several parcels with large FC changes were disconnected from the main graph. Thus, we selected the 0.2% connection threshold to display all findings (Fig. 3 and *SI Appendix*, Fig. S2).

Functional Connectivity Changes by Network. To test which functional networks showed large changes in FC with L-SM1$_{ue}$ during casting, parcel-wise L-SM1$_{ue}$ seed maps were compared with individual-specific network maps. Parcel-wise L-SM1$_{ue}$ difference seed maps (Cast − Pre) were thresholded to contain the top 5% of parcels showing FC increases/decreases. FC increases (Cast > Pre) and decreases (Cast < Pre) were examined separately. The number of suprathreshold parcels in each cortical network is shown in Fig. 3. A threshold-based approach was necessary because alternative approaches (e.g., averaging FC changes across parcels within each network) do not capture inhomogeneity within each network and may fail to quantify the effect of interest. Alternative thresholds (top 1, 10, and 20%) all yielded similar results (*SI Appendix*, Fig. S3). Networks containing a greater number of FC increases/decreases than expected by chance were identified by comparing the number of suprathreshold parcels found using each participant's true network map with the number of parcels found using spatially permuted network maps (*Statistical Analyses*).

Whole-Brain Analyses of Functional Connectivity Changes. To examine changes in FC between all pairs of cortical, subcortical, and cerebellar vertices/voxels, we computed the magnitude of whole-brain FC change for each vertex/voxel as the sum of squared FC changes between that vertex/voxel and every other gray-matter vertex/voxel (Fig. 4 and *SI Appendix*, Fig. S4). We tested if whole-brain FC change was higher in L-SM1$_{ue}$ than in the rest of the brain by comparing the mean magnitude of whole-brain FC change inside of each participant's true L-SM1$_{ue}$ ROI with the mean magnitude of whole-brain FC change inside of spatially rotated ROIs (*Statistical Analyses*).

Spatial and Temporal Comparisons of Pulses and FC Changes. To generate a parcel-wise map of spontaneous activity pulses, we extracted rs-fMRI time series from every cortical, subcortical, and cerebellar parcel surrounding each detected pulse (13.2 s before to 17.6 s after each pulse peak). Pulse peaks were detected previously (31). We then performed an ANOVA on the extracted time series (*SI Appendix*, Fig. S6*B*). The spatial distribution of ANOVA *F* statistics was compared with the spatial distribution of L-SM1$_{ue}$ FC changes using a correlation across parcels. Because FC measures from neighboring parcels are not independent measurements, the correlation values were compared with null distributions generated by rotating one cortical surface relative to the other to generate a *P* value that appropriately accounted for spatial dependence of measurements (*Statistical Analyses*).

We also compared the number of pulses detected during each rs-fMRI scan (31) with the FC measured between L-SM1$_{ue}$ and L-dACC (*SI Appendix*, Fig. S5*C*), using a correlation.

Pulse Censoring Analyses. To assess the contribution of large, detectable spontaneous activity pulses (>0.4% rs-fMRI signal change) to FC changes observed during casting, frames surrounding each pulse (13.2 s before to 17.6 s after each pulse peak) were excluded from FC calculations. Pulse detection criteria were identical to those used previously (31). We plotted FC measured between L-SM1$_{ue}$ and L-dACC during each session before casting, during casting, and during casting with pulses excluded (Cens; Fig. 5*B*). We compared Cast vs. Pre FC measurements and Cens vs. Cast FC measurements using *t* tests (*Statistical Analyses*). We also generated difference seed maps showing FC changes between L-SM1$_{ue}$ and all cortical parcels due to censoring (Cens − Cast; Fig. 5*C*). Censoring was repeated using a range of pulse detection thresholds (*SI Appendix*, Fig. S7).

Pulse Addition Analyses. To assess the contribution to FC changes of pulses with a hypothetical full magnitude distribution, including pulses that were too small (<0.4% rs-fMRI signal change) to distinguish from ongoing spontaneous

Downloaded at Palestinian Territory, occupied on November 29, 2021

www.manaraa.com

activity fluctuations, we created simulated rs-fMRI time series containing a full distribution of pulses. We first generated a histogram showing the magnitude distribution of detected pulses. Magnitudes were grouped into bins with a width of 0.5% signal change. We then fit a log-normal distribution to the observed pulse magnitudes using a least-squares approach (Fig. 6*A*). This provided an estimate of the full pulse magnitude distribution, including pulses that were too small to detect. We then extracted a mean pulse time series from L-SM1$_{ue}$ and L-dACC by averaging together recordings from each region surrounding all detected pulses (13.2 s before to 17.6 s after each pulse peak). We added the mean pulse time series from L-SM1$_{ue}$ and L-dACC to the baseline (Pre) rs-fMRI time series from each region, drawing pulse magnitudes from the full log-normal distribution (example shown in Fig. 6*B*). The number of pulses added was selected so that the number of large pulses (>0.4% signal change) would match the number of pulses detected in each participant in an average Cast scan. We then computed FC of the baseline time series (Pre) and the time series with added pulses (Sim; Fig. 6*C*). Finally, we applied the same pulse censoring strategy described above to the simulated time series and computed FC after censoring (Cens; Fig. 6*C*). Because pulse magnitudes were drawn from a full log-normal distribution, only a portion of the added pulses were detected and censored. We compared Sim vs. Pre FC measurements, Sim vs. Cast FC measurements, and Cens vs. Sim FC measurements using *t* tests (*Statistical Analyses*). The simulation and censoring procedures were repeated using triangular and exponential magnitude distributions (*SI Appendix*, Fig. S8). We also generated difference seed maps showing FC changes between L-SM1$_{ue}$ and all cortical parcels due to pulse simulation (Sim − Pre; Fig. 6*D* and *SI Appendix*, Fig. S9). These analyses involved adding simulated pulses to all brain regions using mean pulse time series specific to each region. For some regions (e.g., L-dACC, L-insula), the mean pulse time series was a large, positive deflection, similar to the mean pulse time series extracted from L-SM1$_{ue}$. These regions showed increased FC with L-SM1$_{ue}$ as a result of pulse simulation. Other brain regions had flat or negative mean pulse time series and did not show increases in FC with L-SM1$_{ue}$ (Fig. 6*D* and *SI Appendix*, Fig. S9).

Statistical Analyses. All statistical tests were performed identically for each participant. Whenever appropriate, we used simple parametric statistical tests:

- Spatial similarity between anatomical maps was tested using a Pearson correlation across parcels (Nico: degrees of freedom [d.f.] = 566; Ashley: d.f. = 578; Omar: d.f. = 624). Spatial correlations were computed between the following maps:
  - o FC changes during casting (Cast − Pre) vs. FC changes during recovery (Post − Cast; Fig. 2*B*)
  - o FC changes during casting (Cast − Pre) vs. pulse ANOVA (*F* statistic; *SI Appendix*, Fig. S6)
  - o FC changes during casting (Cast − Pre) vs. FC changes due to pulse censoring (Cens − Cast; Fig. 5*C* and *SI Appendix*, Fig. S7)
  - o FC changes due to pulse censoring (Cens − Cast) vs. residual FC changes after pulse censoring (Cens − Pre; *SI Appendix*, Fig. S7)
  - o FC changes during casting (Cast − Pre) vs. FC changes due to simulated pulses (Sim − Pre; Fig. 6*D* and *SI Appendix*, Fig. S9)
- The number of pulses detected during each scan was compared with FC measured between L-SM1$_{ue}$ and L-dACC using a Pearson correlation (Nico: d.f. = 45; Ashley: d.f. = 61; Omar: d.f. = 40; *SI Appendix*, Fig. S6*C*).
- FC between L-SM1$_{ue}$ and L-dACC measured during each session of the Cast period (Nico: n = 13 sessions; Ashley: n = 13; Omar: n = 14) was compared with FC during each session of the Pre period (Nico: n = 10; Ashley: n = 12; Omar: n = 14) using a two-sided, unpaired *t* test (Nico: d.f. = 21; Ashley: d.f. = 23; Omar: d.f. = 26; *SI Appendix*, Fig. S6*B*).
- FC between L-SM1$_{ue}$ and L-dACC measured using the full time series (motion-censored only) of each session of the Cast period (Nico: n = 13 sessions; Ashley: n = 13; Omar: n = 14) was compared with FC measurements of the same sessions excluding pulses (motion- and pulse-censored) using a two-sided, paired *t* test (Nico: d.f. = 24; Ashley: d.f. = 24; Omar: d.f. = 26; Fig. 5*B*).
- FC between L-SM1$_{ue}$ and L-dACC measured during each session of the Pre period (Nico: n = 10; Ashley: n = 12; Omar: n = 14) was compared with FC measurements of the same sessions after adding simulated pulses using a two-sided, paired *t* test (Nico: d.f. = 18; Ashley: d.f. = 22; Omar: d.f. = 26; Fig. 6*C*).
- FC between L-SM1$_{ue}$ and L-dACC measured using the full time simulated series (Sim; motion-censored only; Nico: n = 10; Ashley: n = 12; Omar: n = 14) was compared with FC measurements of the same sessions excluding pulses (motion- and pulse-censored) using a two-sided, paired *t* test (Nico: d.f. = 18; Ashley: d.f. = 22; Omar: d.f. = 26; Fig. 6*C*).

When parametric statistical tests were not appropriate to test a specific hypothesis, we tested results against a null distribution generated via permutation resampling. In each case, our null hypothesis was that observed effects had no spatial relationship to ROIs/functional networks and any overlap occurred by chance. For vertex-wise ROIs, we modeled the null hypothesis by rotating the ROI around the cortical surface 1,000 times (47, 48). For functional networks, we modeled the null hypothesis by permuting the network assignments of parcels 1,000 times. Each permuted ROI/network map was used exactly as the actual map in order to compute a null distribution for the value of interest. The *P* value reported for each test represents the two-sided probability that a value in the null distribution has a greater magnitude than the observed value. Permutation resampling was used to generate null distributions for the following values:

- Overlap of each functional network with increases in L-SM1$_{ue}$ FC during casting (Cast > Pre; number of parcels in the top 5%; Fig. 3*B*)
- Overlap of each functional network with decreases in L-SM1$_{ue}$ FC during casting (Cast < Pre; number of parcels in the top 5%; Fig. 3*C*)
- Magnitude of whole-brain FC change in the L-SM1$_{ue}$ ROI (Fig. 4*B* and *SI Appendix*, Fig. S4)
- Spatial correlations between seed maps (Figs. 2*B*, 5*C*, and 6*D* and *SI Appendix*, Figs. S6, S7, and S9)

Since we tested the overlap of L-SM1$_{ue}$ FC increases/decreases with 17 different functional networks, a Benjamini–Hochberg procedure was applied to correct for multiple comparisons, maintaining false discovery rates (FDRs) <0.05. Each of the three participants constituted a separate replication of the experiment, rather than multiple comparisons, so no correction was necessary for tests repeated in each participant.

Data Visualization. Regions of interest and whole-brain pulse maps were shown on cortical surfaces generated by FreeSurfer (45) and the Human Connectome Project (HCP) Workbench software packages (49). These images were rendered using HCP Workbench (49). Figures showing the greatest differences in functional connectivity across the entire brain in inflated anatomical space (Fig. 4 and *SI Appendix*, Fig. S4) were rendered using Blender, a free and open-source three-dimensional modeling software package (http://www.blender.org/). To make the large number of changed connections included in these images visually compact, connections following similar spatial trajectories were drawn toward each other using a previously published mean-shift edge-bundling algorithm (50). All other figures were produced using Matlab (https://www.mathworks.com/).

Data Availability. Anonymized neuroimaging data reported in this article have been deposited in the OpenNeuro database (10.18112/openneuro.ds002766.v3.0.2). This study used our previously published dataset (31), available in the OpenNeuro database (https://openneuro.org/datasets/ds002766). All code needed to reproduce our analyses is available at Gitlab (https://gitlab.com/DosenbachGreene/cast-whole-brain).

ACKNOWLEDGMENTS. We thank Kristen M. Scheidter and Annie L. Nguyen for help in collecting MRI data and Ryan V. Raut for his comments on the manuscript. This work was supported by NIH Grants NS110332 (to D.J.N.), NS088590 (to N.U.F.D.), TR000448 (to N.U.F.D.), MH124567 (to N.U.F.D.), MH096773 (to N.U.F.D.), MH122066 (to N.U.F.D.), MH1000872 (to T.O.L.), MH112473 (to T.O.L.), NS090978 (to B.P.K.), MH104592 (to D.J.G.), NS080675 (to M.E.R.), and NS098577 (to the Neuroimaging Informatics and Analysis Center); US Department of Veterans Affairs Clinical Sciences Research and Development Service Grant 1IK2CX001680 (to E.M.G.); the Kiwanis Neuroscience Research Foundation (N.U.F.D.); Jacobs Foundation Grant 2016121703 (to N.U.F.D.); the Child Neurology Foundation (N.U.F.D.); the McDonnell Center for Systems Neuroscience (D.J.N., T.O.L., A.Z., B.L.S., and N.U.F.D.); the McDonnell Foundation (S.E.P.); Mallinckrodt Institute of Radiology Grant 14-011 (to N.U.F.D.); and the Hope Center for Neurological Disorders (N.U.F.D., B.L.S., and S.E.P.).

1. T. N. Wiesel, D. H. Hubel, Comparison of the effects of unilateral and bilateral eye closure on cortical unit responses in kittens. *J. Neurophysiol.* **28**, 1029–1040 (1965).
2. M. M. Merzenich *et al.*, Topographic reorganization of somatosensory cortical areas 3b and 1 in adult monkeys following restricted deafferentation. *Neuroscience* **8**, 33–55 (1983).
3. G. W. Milliken, E. J. Plautz, R. J. Nudo, Distal forelimb representations in primary motor cortex are redistributed after forelimb restriction: A longitudinal study in adult squirrel monkeys. *J. Neurophysiol.* **109**, 1268–1282 (2013).
4. D. E. Feldman, M. Brecht, Map plasticity in somatosensory cortex. *Science* **310**, 810–815 (2005).

NEUROSCIENCE
Downloaded at Palestinian Territory, occupied on November 29, 2021
www.manaraa.com

5. D. S. Bassett, M. S. Gazzaniga, Understanding complexity in the human brain. *Trends Cogn. Sci.* **15**, 200–209 (2011).
6. M. I. Posner, S. E. Petersen, The attention system of the human brain. *Annu. Rev. Neurosci.* **13**, 25–42 (1990).
7. M. E. Raichle *et al*., A default mode of brain function. *Proc. Natl. Acad. Sci. U.S.A.* **98**, 676–682 (2001).
8. G. L. Shulman, J. M. Ollinger, M. Linenweber, S. E. Petersen, M. Corbetta, Multiple neural correlates of detection in the human brain. *Proc. Natl. Acad. Sci. U.S.A.* **98**, 313–318 (2001).
9. B. Biswal, F. Z. Yetkin, V. M. Haughton, J. S. Hyde, Functional connectivity in the motor cortex of resting human brain using echo-planar MRI. *Magn. Reson. Med.* **34**, 537–541 (1995).
10. M. D. Fox *et al*., The human brain is intrinsically organized into dynamic, anticorrelated functional networks. *Proc. Natl. Acad. Sci. U.S.A.* **102**, 9673–9678 (2005).
11. M. D. Greicius, B. Krasnow, A. L. Reiss, V. Menon, Functional connectivity in the resting brain: A network analysis of the default mode hypothesis. *Proc. Natl. Acad. Sci. U.S.A.* **100**, 253–258 (2003).
12. B. T. Yeo *et al*., The organization of the human cerebral cortex estimated by intrinsic functional connectivity. *J. Neurophysiol.* **106**, 1125–1165 (2011).
13. J. D. Power *et al*., Functional network organization of the human brain. *Neuron* **72**, 665–678 (2011).
14. D. Cordes *et al*., Frequencies contributing to functional connectivity in the cerebral cortex in "resting-state" data. *AJNR Am. J. Neuroradiol.* **22**, 1326–1333 (2001).
15. M. J. Lowe, B. J. Mock, J. A. Sorenson, Functional connectivity in single and multislice echoplanar imaging using resting-state fluctuations. *Neuroimage* **7**, 119–132 (1998).
16. M. D. Fox, M. Corbetta, A. Z. Snyder, J. L. Vincent, M. E. Raichle, Spontaneous neuronal activity distinguishes human dorsal and ventral attention systems. *Proc. Natl. Acad. Sci. U.S.A.* **103**, 10046–10051 (2006).
17. W. W. Seeley *et al*., Dissociable intrinsic connectivity networks for salience processing and executive control. *J. Neurosci.* **27**, 2349–2356 (2007).
18. N. U. Dosenbach *et al*., Distinct brain networks for adaptive and stable task control in humans. *Proc. Natl. Acad. Sci. U.S.A.* **104**, 11073–11078 (2007).
19. N. U. Dosenbach, D. A. Fair, A. L. Cohen, B. L. Schlaggar, S. E. Petersen, A dual-networks architecture of top-down control. *Trends Cogn. Sci.* **12**, 99–105 (2008).
20. S. Marek, N. U. F. Dosenbach, Control networks of the frontal lobes. *Handb. Clin. Neurol.* **163**, 333–347 (2019).
21. N. U. Dosenbach *et al*., A core system for the implementation of task sets. *Neuron* **50**, 799–812 (2006).
22. E. M. Gordon *et al*., Precision functional mapping of individual human brains. *Neuron* **95**, 791–807.e7 (2017).
23. T. O. Laumann *et al*., Functional system and areal organization of a highly sampled individual human brain. *Neuron* **87**, 657–670 (2015).
24. D. Wang *et al*., Parcellating cortical functional networks in individuals. *Nat. Neurosci.* **18**, 1853–1860 (2015).
25. S. Mueller *et al*., Individual variability in functional connectivity architecture of the human brain. *Neuron* **77**, 586–595 (2013).
26. S. Marek *et al*., Spatial and temporal organization of the individual human cerebellum. *Neuron* **100**, 977–993.e7 (2018).
27. D. J. Greene *et al*., Integrative and network-specific connectivity of the basal ganglia and thalamus defined in individuals. *Neuron* **105**, 742–758.e6 (2020).
28. R. M. Braga, R. L. Buckner, Parallel interdigitated distributed networks within the individual estimated by intrinsic functional connectivity. *Neuron* **95**, 457–471.e5 (2017).
29. R. A. Poldrack *et al*., Long-term neural and physiological phenotyping of a single human. *Nat. Commun.* **6**, 8885 (2015).
30. C. M. Sylvester *et al*., Individual-specific functional connectivity of the amygdala: A substrate for precision psychiatry. *Proc. Natl. Acad. Sci. U.S.A.* **117**, 3808–3818 (2020).
31. D. J. Newbold *et al*., Plasticity and spontaneous activity pulses in disused human brain circuits. *Neuron* **107**, 580–589.e6 (2020).
32. J. D. Power, K. A. Barnes, A. Z. Snyder, B. L. Schlaggar, S. E. Petersen, Spurious but systematic correlations in functional connectivity MRI networks arise from subject motion. *Neuroimage* **59**, 2142–2154 (2012).
33. C. Gratton *et al*., Emergent functional network effects in Parkinson disease. *Cereb. Cortex* **29**, 2509–2523 (2019).
34. M. D. Greicius *et al*., Resting-state functional connectivity in major depression: Abnormally increased contributions from subgenual cingulate cortex and thalamus. *Biol. Psychiatry* **62**, 429–437 (2007).
35. T. Harmelech, R. Malach, Neurocognitive biases and the patterns of spontaneous correlations in the human cortex. *Trends Cogn. Sci.* **17**, 606–615 (2013).
36. B. Guerra-Carrillo, A. P. Mackey, S. A. Bunge, Resting-state fMRI: A window into human brain plasticity. *Neuroscientist* **20**, 522–533 (2014).
37. C. M. Lewis, A. Baldassarre, G. Committeri, G. L. Romani, M. Corbetta, Learning sculpts the spontaneous activity of the resting human brain. *Proc. Natl. Acad. Sci. U.S.A.* **106**, 17558–17563 (2009).
38. B. J. Shannon *et al*., Brain aerobic glycolysis and motor adaptation learning. *Proc. Natl. Acad. Sci. U.S.A.* **113**, E3782–E3791 (2016).
39. S. E. Petersen, M. I. Posner, The attention system of the human brain: 20 years after. *Annu. Rev. Neurosci.* **35**, 73–89 (2012).
40. M. Neta, S. M. Nelson, S. E. Petersen, Dorsal anterior cingulate, medial superior frontal cortex, and anterior insula show performance reporting-related late task control signals. *Cereb. Cortex* **27**, 2154–2165 (2017).
41. C. L. Wellman, L. L. Arnold, E. E. Garman, P. E. Garraghty, Acute reductions in GABAA receptor binding in layer IV of adult primate somatosensory cortex after peripheral nerve injury. *Brain Res.* **954**, 68–72 (2002).
42. E. M. Gordon *et al*., Three distinct sets of connector hubs integrate human brain function. *Cell Rep.* **24**, 1687–1695.e4 (2018).
43. Z. P. Rosenthal *et al*., Local perturbations of cortical excitability propagate differentially through large-scale functional networks. *Cereb. Cortex* **30**, 3352–3369 (2020).
44. R. V. Raut, A. Mitra, A. Z. Snyder, M. E. Raichle, On time delay estimation and sampling error in resting-state fMRI. *Neuroimage* **194**, 211–227 (2019).
45. B. Fischl, FreeSurfer. *Neuroimage* **62**, 774–781 (2012).
46. M. Jacomy, T. Venturini, S. Heymann, M. Bastian, ForceAtlas2, a continuous graph layout algorithm for handy network visualization designed for the Gephi software. *PLoS One* **9**, e98679 (2014).
47. E. M. Gordon *et al*., Generation and evaluation of a cortical area parcellation from resting-state correlations. *Cereb. Cortex* **26**, 288–303 (2016).
48. E. M. Gordon *et al*., Default-mode network streams for coupling to language and control systems. *Proc. Natl. Acad. Sci. U.S.A.* **117**, 17308–17319 (2020).
49. D. S. Marcus *et al*., Informatics and data mining tools and strategies for the Human Connectome Project. *Front. Neuroinform.* **5**, 4 (2011).
50. J. Böttger, A. Schäfer, G. Lohmann, A. Villringer, D. S. Margulies, Three-dimensional mean-shift edge bundling for the visualization of functional connectivity in the brain. *IEEE Trans. Vis. Comput. Graph.* **20**, 471–480 (2014).

Downloaded at Palestinian Territory, occupied on November 29, 2021

www.manaraa.com